

## High terrestrial temperature in the low-latitude Nanxiong Basin during the Cretaceous-Paleogene boundary interval

Yitian Yin <sup>a</sup>, Laiming Zhang <sup>a,\*</sup>, Xue Gu <sup>a</sup>, Runsheng Yin <sup>b</sup>, Yixiong Wen <sup>a</sup>, Tianjie Jin <sup>a</sup>, Chengshan Wang <sup>a</sup>

<sup>a</sup> State Key Laboratory of Biogeology and Environmental Geology and School of Earth Sciences and Resources, China University of Geosciences (Beijing), Beijing, China

<sup>b</sup> State Key Laboratory of Ore Deposit Geochemistry, Institute of Geochemistry, Chinese Academy of Sciences, Guiyang, China



### ARTICLE INFO

Editor: A Dickson.

**Keywords:**

Clumped isotopes  
K-Pg boundary interval  
Terrestrial temperature  
Low latitudes  
Mercury concentration

### ABSTRACT

As CO<sub>2</sub> keeps emitting, it is urgent to project future climatic changes by quantitatively reconstructing deep time paleoclimate in high atmospheric CO<sub>2</sub> concentrations. However, there are still unneglected discrepancies between the terrestrial temperatures based on the climatic proxies and climate models, especially at low latitudes, which limits our interpretation of the terrestrial responses to global climate changes at low latitudes. In this study, the clumped isotope concentrations ( $\Delta_{47}$ ) and total mercury signals are analyzed for the uppermost Cretaceous-lowermost Paleogene strata in the low-latitude Nanxiong Basin, South China. After excluding the potential diagenesis by both recrystallization and solid-state reordering, our study presents an extremely high mean annual terrestrial temperature of ca. 30 °C in the low latitudes. Our result is significantly higher than the previous estimates and supports a hot and expanded tropics during the latest Cretaceous-earliest Paleocene (i.e., K-Pg boundary interval). In addition, we suggest that the hot climate was plausibly caused by Deccan Traps (DT) volcanism, although the mercury concentrations in the section show relatively low peaks during the main eruptions. We speculate that the mercury sequestration in the Nanxiong Basin may have been affected by the extremely hot and arid regional climate.

### 1. Introduction

Quantitative reconstruction of past greenhouse temperatures using proper proxies provides critical insights into Earth's response to rising greenhouse gas levels and helps to examine the accuracy of available climate models (Naafs et al., 2018; Tierney et al., 2020; Upchurch et al., 2015). The K-Pg boundary interval was a relatively "cool" period with multiple climatic fluctuations between two typical hothouse period (i.e., the mid-Cretaceous and the Early Paleogene) (Green et al., 2022; Scoteese, 2021; Tierney et al., 2020). Synthetically affected by DT eruptions and the asteroid impact event (Barnet et al., 2017; Gilabert et al., 2022; Green et al., 2022; Gu et al., 2022), both the pCO<sub>2</sub> and global mean surface temperature rapidly increased by 1000–2000 ppm and 3–5 °C during this interval, respectively (Hull et al., 2020; Milligan et al., 2022; Westerhold et al., 2020; Zhang et al., 2018). While studies have conducted paleoclimate reconstructions on the marine sections and mid- to high-latitude terrestrial sections, our knowledge of low-latitude terrestrial paleoclimate remains insufficient during the interval. Among the

previous studies, only Amiot et al. (2004) suggested a terrestrial temperature of 18 °C at low latitudes based on vertebrate apatite  $\delta^{18}\text{O}$ , which is much lower than the estimates (up to 40 °C) based on climate modeling (Niezgodzki et al., 2017). More work on reconstruction of low-latitude terrestrial paleoclimate is warranted to verify such contradiction, based on proper selection of paleotemperature proxies (Huber, 2008; Wang, 2006).

The newly developed clumped isotopes ( $\Delta_{47}$ ) thermometry is increasingly used as a powerful tool to reconstruct terrestrial temperatures during greenhouse periods due to their ability to quantitatively resolve the upper thermal limits (Jones et al., 2022; Petersen et al., 2016; Zhang et al., 2018). It measures the amount of  $^{13}\text{C}-^{18}\text{O}$  bonds within the carbonate lattice (Ghosh et al., 2006) and directly estimates the paleotemperature without assuming the water  $\delta^{18}\text{O}$  ( $\delta^{18}\text{O}_{\text{water}}$ ) (Passey et al., 2010). Here, clumped isotopes ( $\Delta_{47}$ ) thermometry was used to pedogenic carbonates in the Nanxiong Basin, South China (paleolatitude was ~25°N) to reconstruct the low-latitude terrestrial paleotemperature during the latest Cretaceous-earliest Paleogene

\* Corresponding author.

E-mail address: [lzhang@cugb.edu.cn](mailto:lzhang@cugb.edu.cn) (L. Zhang).

(70–64 Ma). In addition, mercury (Hg) concentrations of the samples were measured to evaluate the impact of DT eruption in the Nanxiong Basin, given Hg anomalies in sediments are indicative of large volcanism (Grasby et al., 2019). Results of this study would help to refine our understanding of tropical terrestrial paleoclimate during the K-Pg boundary interval.

## 2. Geological contexts

As a small intermontane basin, the Nanxiong Basin in South China is famous for its abundant dinosaur eggs and eggshells fractions (Fig. 1a) (Clyde et al., 2010). Based on the paleogeography reconstructions, the location of the Nanxiong Basin is unchanged and the paleolatitude was  $\sim 25^{\circ}\text{N}$  during the Late Cretaceous (see <http://www.earthbyte.org/paleodem-resourcescote-and-wright-2018>). In this basin, the relatively continuous Upper Cretaceous to Lower Paleocene fluvial-lacustrine strata are well preserved (Yan et al., 2007). From bottom to top, the sedimentary cover varies from Upper Cretaceous Zhutian and Zhenshui formations to Lower Paleogene Shanghu Formation (Zhang et al., 2006; Zhang et al., 2013). Samples studied were taken from the Datang section, starting at Yangmeikeng and ending at Nilongkeng, in the northeastern of the Nanxiong Basin, with a thickness of 700 m (Zhang et al., 2006) (Fig. 1a). In the Datang section, many layers of paleosol are identified (Clyde et al., 2010), which represents the short-lived hiatus of deposition (i.e., 2,000–30,000 years) (Kraus, 1999).

In the Nanxiong Basin, the age model is established by the geomagnetic polarity sequences, biostratigraphic data, and isotopic geochemical data ( $\delta^{13}\text{C}$  and  $\delta^{18}\text{O}$ ) (Fig. 1b and c) (Clyde et al., 2010; Li

et al., 2010; Ma et al., 2018; Wang, 2012; Zhang et al., 2006). According to the appearance/disappearance of mammals and non-avian dinosaurs (Zhang et al., 2006) and the excursions of the stable isotopes (Clyde et al., 2010), the previous studies tentatively placed the K-Pg boundary to the boundary between the Zhenshui and Shanghu formations (400 m). Recently, A paleomagnetic study validated the above-mentioned location of the K-Pg boundary, and concluded that the strata range from 71.9 to 62.8 Ma in the Datang section (Ma et al., 2018) (Fig. 1b). In this study, the specific ages of our samples are interpolated by assuming consistent depositional rate in each magnetozone (Fig. 1b).

## 3. Materials and methods

### 3.1. Clumped isotope analysis

Carbonate nodules  $>1\text{ cm}$  in diameter were collected for the  $\Delta_{47}$  analysis (Fig. 1b). For each sample,  $\sim 100\text{ mg}$  carbonate powder was drilled from the polished carbonate nodule surface.  $\Delta_{47}$ ,  $\delta^{18}\text{O}$ , and  $\delta^{13}\text{C}$  were measured concurrently with two to three replicates per sample at Johns Hopkins University, following the methods described in Passey et al. (2010). For each replicate analysis,  $\sim 10\text{--}15\text{ mg}$  carbonate powder acidified in a common bath of  $90^{\circ}\text{C}$  phosphoric acids for  $\sim 10\text{ min}$  and the generated  $\text{CO}_2$  was purified by passage through a series of cryogenic traps. Intra-laboratory carbonate standards were analyzed to monitor long-term analytical error.  $\Delta_{47}$  values were calculated using IUPAC parameters to correct for  $^{17}\text{O}$  mass interference. The calibration of Anderson et al. (2021) was used to generate  $T(\Delta_{47})$ :  $\Delta_{47}(\text{I-CDES90}^{\circ}\text{C}) = (0.0391 \pm 0.0004) \times (10^6/T^2) + (0.154 \pm 0.004)$  [T in kelvin]. The

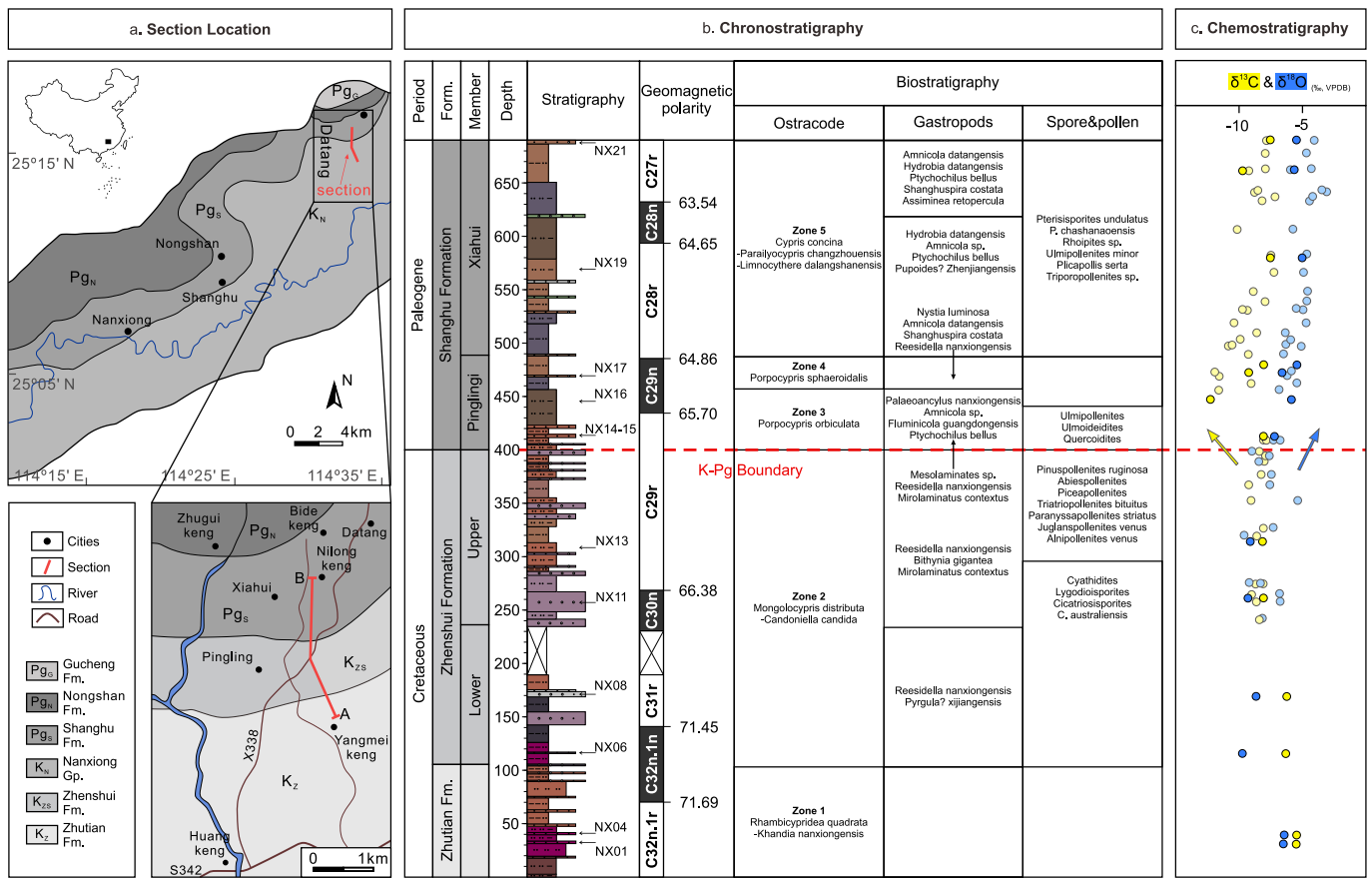


**Fig. 1.** Geological setting of the Nanxiong Basin. (a) A schematic geological map shows the location of the Datang section. (b) Integrated lithological column shows the K-Pg boundary at  $\sim 400\text{ m}$  in depth. Our samples are plotted next to lithological column. The biostratigraphy stratigraphy is derived from Zhang et al. (2006). (c) The  $\delta^{13}\text{C}$  (yellow circles) and  $\delta^{18}\text{O}$  (blue circles) of paleosol carbonates in the Nanxiong Basin. The darker ones come from this study and the paler ones come from Clyde et al. (2010). Notice the negative/positive shift of the  $\delta^{13}\text{C}/\delta^{18}\text{O}$  at the K-Pg boundary. This figure is modified after Clyde et al. (2010) and Ma et al. (2018). (For interpretation of the references to colour in this figure legend, the reader is referred to the web version of this article.)

subscript CDES means carbon dioxide equilibrium scale (CDES) (Dennis et al., 2011). The external standard error (1SE) in  $\Delta_{47}$  analyses is calculated as the standard deviation of carbonate sample replicates (or long-term standard deviation of carbonate standard analyses if it is larger) divided by the square root of the number of replicates for each sample. Soil water  $\delta^{18}\text{O}_{\text{water}}$  values were calculated from the clumped temperatures  $T(\Delta_{47})$  and soil carbonate  $\delta^{18}\text{O}$  values.

### 3.2. Mercury concentration analysis

Mercury concentration ( $n = 131$ ) was measured at the Institute of Geochemistry, Chinese Academy of Sciences, Guiyang, China. ~150 mg powder per sample was transferred to the combustion boat and heated to 800 °C, then analyzed by using a DMA80 Direct Mercury Analyzer (Milestone). The sampling resolution is 0.7 m during 360–420 m in depth ( $n = 49$ ) (Ma et al., 2018; Zhao et al., 2021) and 2–10 m for other depths ( $n = 82$ ). Data accuracy was confirmed by the analysis of one certified reference material (GSS-5, soil, 290 ppb Hg) and one replicate sample for every ten samples, yielding uncertainty of <10% (2SD) for Hg concentrations reported.

### 3.3. Major element analysis

The major element analysis ( $n = 131$ ) was conducted using the Zsx Primus II wavelength dispersive X-ray fluorescence spectrometer (XRF) at the Wuhan SampleSolution Analytical Technology Co., Ltd., Wuhan, China. The pretreatment was made by melting method at 1050 °C for 15 min. The flux is a mixture of lithium tetraborate, lithium metaborate, and lithium fluoride (45: 10: 5). The ammonium nitrate and lithium bromide were used as oxidant and release agent, respectively. The X-ray tube is a 4.0 Kw end window Rh target with 50 kV voltage and 60 mA current. The standard curve uses the national standard material GBW07101–14. The data are corrected by the theoretical  $\alpha$  coefficient method and the relative standard deviation (RSD) is <2%.

## 4. Results

### 4.1. Clumped isotopes

The samples investigated show  $\delta^{13}\text{C}$  values ranging from −12.6‰ to −5.4‰ and  $\delta^{18}\text{O}$  values ranging from −9.0‰ to −4.9‰. The trends of  $\delta^{18}\text{O}$  and  $\delta^{13}\text{C}$  are similar with previous observations in the K-Pg boundary interval in East Asia. Generally, the  $\delta^{18}\text{O}$  values display an upward increasing trend, while the  $\delta^{13}\text{C}$  values display an upward decreasing trend, associating with abrupt positive/negative  $\delta^{18}\text{O}/\delta^{13}\text{C}$  excursions at the K-Pg boundary, respectively (Fig. 1c) (Clyde et al., 2010; Gao et al., 2015; Huang et al., 2013). The  $\Delta_{47}$  values range from 0.525‰ to 0.617‰ and yield apparent  $T(\Delta_{47})$  values range from 17 ± 4 °C to 52 ± 5 °C (1 SE) (Table 1). The calculated  $\delta^{18}\text{O}_{\text{water}}$  values range from −5.3‰ to 0.0‰. Some of the  $T(\Delta_{47})$  far exceeds the reasonable Earth-surface temperature (i.e., 40 °C), which may be caused by post-depositional diagenesis and should not represent initial forming temperatures. The complete data are reported in Dataset S1.

### 4.2. Mercury concentrations

Total Hg concentrations (THg) of the Zhutian and Shanghu formations show relatively constant background value of ~1 ppb (Fig. 2a). Some samples at the K-Pg boundary show relatively higher values of 2 to 10 ppb. As organic matter (OM) and clay minerals mainly controlled the amount of Hg sequestered in terrestrial sediments (Gu et al., 2022; Kongchum et al., 2011), normalization by TOC and  $\text{Al}_2\text{O}_3$  contents could help to understand the principal host phases of sedimentary Hg (Font et al., 2016; Percival et al., 2015). Practically, for those samples with low TOC content (<0.2 wt%), their Hg/TOC values will be artificial high and should not be used (Grasby et al., 2019). For the Nanxiong Basin, THg shows no significant correlation with either TOC or  $\text{Al}_2\text{O}_3$ . All the TOC values of the uppermost Cretaceous-lowermost Paleogene strata are generally low (i.e., <0.1%) (Zhao et al., 2021), which suggests that the Hg concentrations was not regulated by OM sequestration in this study. Besides, the  $\text{Al}_2\text{O}_3$  contents, ranging from 10 to 20%, also show relatively uniform values for all the samples (Fig. 2b). The complete data are reported in Dataset S2.

**Table 1**  
Results of clumped isotope analyses.

Sample ID	Age (Ma)	N <sup>a</sup>	$\delta^{13}\text{C}^{\text{b}}$ (‰, VPDB)	$\delta^{18}\text{O}^{\text{b}}$ (‰, VPDB)	$\Delta_{47}^{\text{c}}$ (‰, CDES)	$T(\Delta_{47})^{\text{d}}$ (°C)	$\delta^{18}\text{O}_{\text{water}}^{\text{e}}$ (‰, VSMOW)
<i>Spar</i>							
NX-01	71.86	2	−5.8	−6.1	0.613 (0.005)	19 (5)	−5.0
NX-04	71.82	2	−5.4	−6.1	0.617 (0.007)	17 (4)	−5.3
NX-16	65.52	3	−12.6	−6.0	0.614 (0.004)	18 (4)	−5.0
Average <sup>f</sup>		8		−6.1	0.615 (0.007)	18 (2)	−5.1
<i>Microspar</i>							
NX-06	71.53	2	−5.9	−7.5	0.527 (0.014)	51 (6)	−0.4
NX-08	70.30	2	−8.1	−9.0	0.532 (0.005)	49 (6)	−2.2
NX-11	66.64	3	−8.2	−8.7	0.534 (0.008)	48 (5)	−2.0
NX-13	66.19	3	−8.3	−8.9	0.547 (0.010)	42 (5)	−3.2
NX-14	65.79	3	−8.4	−7.4	0.525 (0.005)	52 (5)	0.0
Average <sup>f</sup>		13		−8.3	0.534 (0.006)	48 (2)	−1.7
<i>Dense micrite</i>							
NX-15	65.79	3	−7.7	−7.0	0.576 (0.007)	31 (4)	−3.4
NX-17	65.11	3	−9.4	−6.4	0.565 (0.004)	35 (4)	−2.0
NX-19	64.68	2	−7.3	−4.9	0.558 (0.004)	38 (5)	0.0
NX-21	62.84	2	−7.5	−5.5	0.551 (0.003)	41 (6)	−0.1
Average <sup>f</sup>		10		−6.1	0.564 (0.006)	36 (2)	−1.6

<sup>a</sup> Number of replicates of clumped isotope analyses.

<sup>b</sup>  $\delta^{13}\text{C}$  and  $\delta^{18}\text{O}$  standard errors from sample replicates are <0.07‰ and 0.06‰, respectively.

<sup>c</sup> CDES = Carbon dioxide equilibrium scale. Acid correction factor = 0.0‰. Uncertainties are reported in parentheses. SE = SD/SQRT (N). If SD is less than the long-term standard deviation of carbonate standard analyses (0.020‰), then 0.020‰ is used.

<sup>d</sup> Calculated using Eq. (1) in Anderson et al. (2021). Uncertainties are reported in parentheses.

<sup>e</sup> Calculated using the equation for calcite reported in Kim and O'Neil (1997).

<sup>f</sup> The weighted-average temperature and error are calculated from the replicate-level data. See Dataset S1 for details.

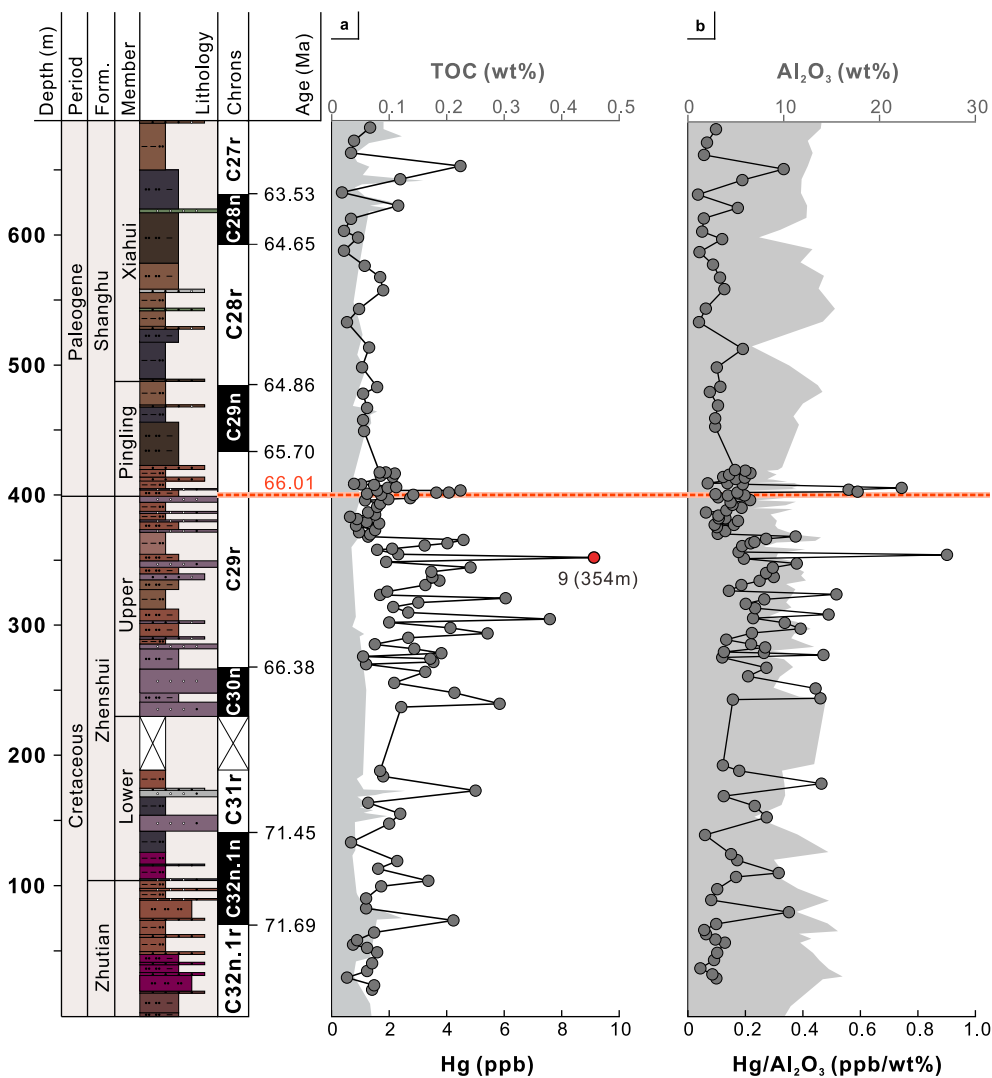


**Fig. 2.** The Mercury concentrations for the Nanxiong Basin. (a) THg (black dot) and TOC (gray shadow). The red dot represents the highest THg value (9 ppb at 354 m). TOC values are derived from Zhao et al. (2021). (b)  $\text{Hg}/\text{Al}_2\text{O}_3$  (black dot) and  $\text{Al}_2\text{O}_3$  (gray shadow). The red horizontal line represents the K-Pg boundary (400 m) (Ma et al., 2018). Form. = Formation. The complete data are reported in Dataset S2. (For interpretation of the references to colour in this figure legend, the reader is referred to the web version of this article.)

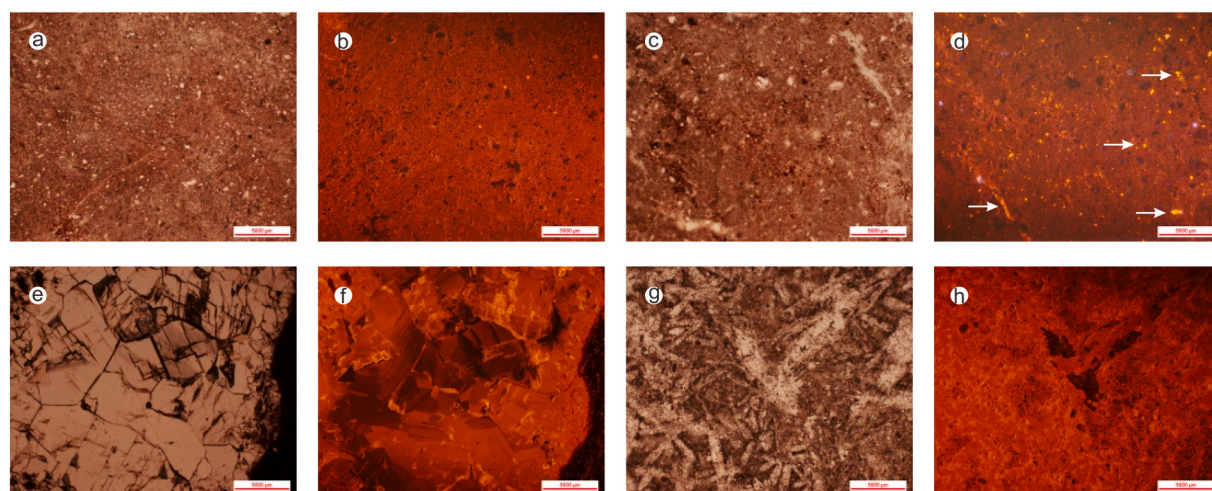


**Fig. 3.** Optical and cathodoluminescence petrographic photos of (a-b) dense micrites, (c-d) microspars, and (e-h) spars. Scale bars for all images are 5000  $\mu\text{m}$ .

## 5. Discussions

### 5.1. Diagenesis

Post-depositional diagenesis could modify both the clumped and carbon and oxygen isotopes of authigenic carbonates, thus erasing the original information regarding the depositional environment and limiting the use of isotopic proxies to reconstruct paleoclimate (Huntington and Lechler, 2015; Inglis et al., 2015). In this study, the apparent  $T(\Delta_{47})$  values range from 17 to 52 °C, which indicates that some of the apparent temperatures could be primary whereas others far exceed the reasonable Earth-surface temperature (i.e., <40 °C) and must be diagenetically altered. Here, we employ detailed petrographic analyses and solid-state reordering models to assess possible diagenetic alteration.

#### 5.1.1. Assessing potential diagenesis by recrystallization

The  $\Delta_{47}$  recorded by minerals undergone recrystallization reflect the temperature at which recrystallization occurred, with calcite recrystallization being more responsive to changes in burial temperatures (John, 2018; Robinson et al., 2022). Under optical and cathodoluminescence (CL) microscope examinations, three petrographic categories (i.e., spar, dense micrite, and microspar) are classified according to the extent of recrystallization (Fig. 3). They show different  $\Delta_{47}$  temperature ranges as ~17–19 °C for the spar samples, ~31–41 °C for the dense micrite samples, and ~42–52 °C for the microspar samples, respectively (Fig. 4a).

For the dense micrite samples, both the optical and CL features indicate that they are dominated by dense and homogeneous micrites, with sporadic veins and grains of non-luminescent siliciclastic (mostly quartz) material (Fig. 3a and b). Following previous studies (Drise and Mora, 1993; Snell et al., 2013; Zhang et al., 2021), we conclude that the dense micrite samples archived the original clumped isotope compositions and their apparent  $T(\Delta_{47})$  values, range from 31 to 41 °C, represent the Earth-surface paleoclimate condition in the Nanxiong Basin during the K-Pg boundary interval.

The microspar samples show an irregular pattern of micrite (darker) and mini-spar (lighter). A few isolated specks of luminescent spar occur, which are hardly circumvented during sampling (Fig. 3c and d). Compared to the dense micrite samples, the microspar samples exhibit higher temperatures (e.g., 48 °C in average) and nearly the same  $\delta^{18}\text{O}_{\text{water}}$  values (i.e., -1.7‰ vs -1.6‰ VSMOW in average). For example, in one paleosol layer, the  $\Delta_{47}$  temperature of microspar sample (NX-15) is >20 °C higher than that of the dense micrite sample (NX-14). In this study, assuming a constant oxygen isotope composition of diagenesis fluid, we model the diagenesis process by using the equations in Banner and Hanson (1990). We suggest that the recrystallization occurred in a closed system from a initial temperature of ~37 °C (Fig. 4b), which is consistent to the average apparent  $T(\Delta_{47})$  value (i.e., 36 °C) of the dense micrite samples.

The spar samples show obvious diagenetic features such as sparite specks, dense microspar specks, and large amount of calcite veins, which means they were pervasively recrystallized (Fig. 3e-h). Their  $T(\Delta_{47})$  values (18 °C in average) and  $\delta^{18}\text{O}_{\text{water}}$  values (-5.1‰ in average) are significantly lower than the other petrographic categories (Fig. 4a). In the modern eras, the mean annual temperature is 16–25 °C according to the Global Summary of the Year (GSOY) (Lawrimore et al., 2016) and the weighted average oxygen isotope of precipitation is -5.2‰ according to the Global Network of Isotopes in Precipitation (GNIP) (Chen et al., 2010). The similarity of temperature and  $\delta^{18}\text{O}_{\text{water}}$  between the spar samples and the modern observations implies that these spars may reprecipitate from near-modern meteoric water after denudation.

#### 5.1.2. Assessing potential diagenesis by solid-state reordering

In addition to the recrystallization, at elevated temperatures, solid-state reordering may also affect the  $^{13}\text{C}-^{18}\text{O}$  bonds in carbonate

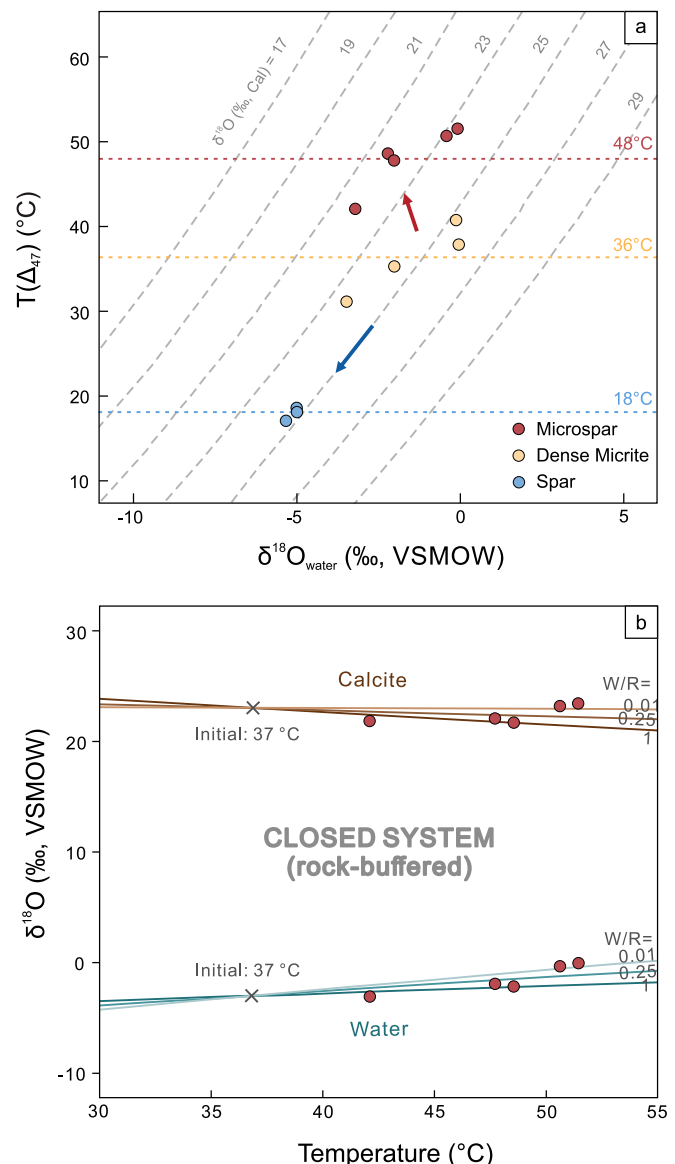


**Fig. 4.** The clumped isotope paleotemperatures  $T(\Delta_{47})$ . (a) Cross-plot of clumped isotope paleotemperatures  $T(\Delta_{47})$  vs oxygen isotopic composition of fluids ( $\delta^{18}\text{O}_{\text{water}}$ ) for the pedogenic carbonates from the Nanxiong Basin. The contours of  $\delta^{18}\text{O}_{\text{Cal}}$  are calculated by equation in Kim and O'Neil (1997). The horizontal dotted lines (red, yellow, and blue) represent the apparent  $T(\Delta_{47})$  for the microspar, dense micrite, and spar samples, respectively. The arrows indicate the diagenesis paths from the initial dense micrite carbonates to the recrystallized ones. (b) The oxygen isotopic evolution of a rock-buffered closed system with different water-to-rock ratios (W/R) at temperatures of 30–55 °C for the microspar samples following the equations in Banner and Hanson (1990). The model assumes an initial  $\delta^{18}\text{O}$  value of -3.0‰ and 23.0‰ (VSMOW) for water and calcite, respectively. (For interpretation of the references to colour in this figure legend, the reader is referred to the web version of this article.)

lattices over geologic time scales, which would decrease  $\Delta_{47}$  and increase  $\delta^{18}\text{O}_{\text{water}}$  values without altering trace element or SEM screening (Passey and Henkes, 2012; Stolper and Eiler, 2015). To distinguish whether or not our dense micrite samples underwent solid-state bond reordering, we model the  $T(\Delta_{47})$  changes during the burial process in the Nanxiong Basin (Henkes et al., 2018; Jones et al., 2022). According to the stratigraphic thickness in the Nanxiong Basin, the burial depth of the Upper Cretaceous strata reached its maximum of 1495–1777 m during the deposition of Eocene Guchengcun Formation (Zhang et al., 2013).

Assuming an initial depositional temperature ( $T_0$ ) of 20–30 °C and a geothermal gradient of 25 °C/km (Xi et al., 2015), the maximum burial temperature ( $T_{\max}$ ) was 65–75 °C. The burial history is inferred from Zhang et al. (2013). We only know that the Nanxiong Basin received continuously deposition for ~16 Myrs and reached the maximum burial temperature ( $T_{\max}$ ). However, we know little about the exhumation history of the Nanxiong Basin, which means we did not know when our samples were exhumed to the Earth surface. Therefore, we assume the maximum burial temperature lasted for 50 Myrs to model an extreme case. The detailed thermal history for the Nanxiong Basin are reported in Dataset S3.

Here, based on the above mentioned temperature-time path, the  $T(\Delta_{47})$  values are further modeled by solid-state reordering using the Python code of Hemingway (2020). The final predicted temperatures in all the model-scenario combinations equal to initial depositional temperatures ( $T_0$ ) with imperceptible differences (<3 °C), which suggests that our dense micrite samples would not be altered by solid-state reordering (Fig. 5). Therefore, we suggest that the dense micrite samples reflect unaltered initial depositional temperatures of 31–41 °C.

## 5.2. High low-latitude temperatures and tropical expansion

The precipitation of calcite in the soil is predominantly favored under the condition of increased temperature and decrease soil moisture after infiltration events (Huth et al., 2019). Generally, the  $\Delta_{47}$  temperatures from paleosol carbonates usually exceed mean annual air temperature (MAAT) due to summer preference and solar heating (Kelson et al., 2020). Here, we conclude that our results are summer biased. First, the  $T(\Delta_{47})$  values of paleosol carbonates in the NE China during this period were also summer biased (Zhang et al., 2016a). Second, the previous study suggested that a monsoon climate had already emerged in East Asia since Late Cretaceous and led to a majority of precipitation

in warm season (Farnsworth et al., 2019).

Burgener et al. (2019) claimed that the seasonality during the Late Cretaceous was nearly no different with the present level. At present, the summer air temperature (SAT) is ~3–5 °C higher than the MAAT in the Nanxiong Basin (Lawrimore et al., 2016). Laugé et al. (2020) and Klages et al. (2020) also suggested that the low-latitude summer air temperature is ~3–5 °C higher than MAAT during the Cretaceous thermal maximum (KTM; early-mid-Turonian). Here, taken the radiative heating of ~0–3 °C into account (Burgener et al., 2019), we arbitrarily conclude that our  $T(\Delta_{47})$  values were  $6 \pm 3$  °C higher than the MAAT in the Nanxiong Basin during the K-Pg boundary interval. Therefore, the average  $T(\Delta_{47})$  value of  $36 \pm 2$  °C leads to an average MAAT of  $30 \pm 4$  °C (1 SE), which is higher than the highest MAAT at present (i.e., ~25–28 °C in North Africa) (Lawrimore et al., 2016).

Most of our  $\Delta_{47}$  temperature records reflect a warm interval of 1–2 Ma posterior to the K-Pg boundary. According to the global temperature compilation by Hull et al. (2020), the global mean temperature did not change much during the K-Pg boundary interval, which is also verified by the high-resolution benthic foraminiferal stable isotope record in Pacific Ocean (Westerhold et al., 2011). Therefore, we suggest that our Dannian temperature records could reflect a general paleoclimate condition during the K-Pg boundary interval, although a high-resolution temperature record is still needed to study the climatic fluctuations.

In such a circumstance (i.e., an average MAAT of ~30 °C and an average SAT of ~36 °C) in low latitudes, some tropical regions must have been even hotter and would occasionally approach a tolerable threshold on land (i.e., 35–40 °C for plants and 45 °C for animals) (Sun et al., 2012). Due to the torrid climate, the terrestrial lives would escape to high-latitude or high-altitude regions, became extinct or spread. With respect to the relatively cool climate in low latitudes (e.g., 18 °C at 25°S) based on the vertebrate apatite  $\delta^{18}\text{O}$  reported by Amiot et al. (2004), we suggest that the intolerably high temperatures may not be archived since

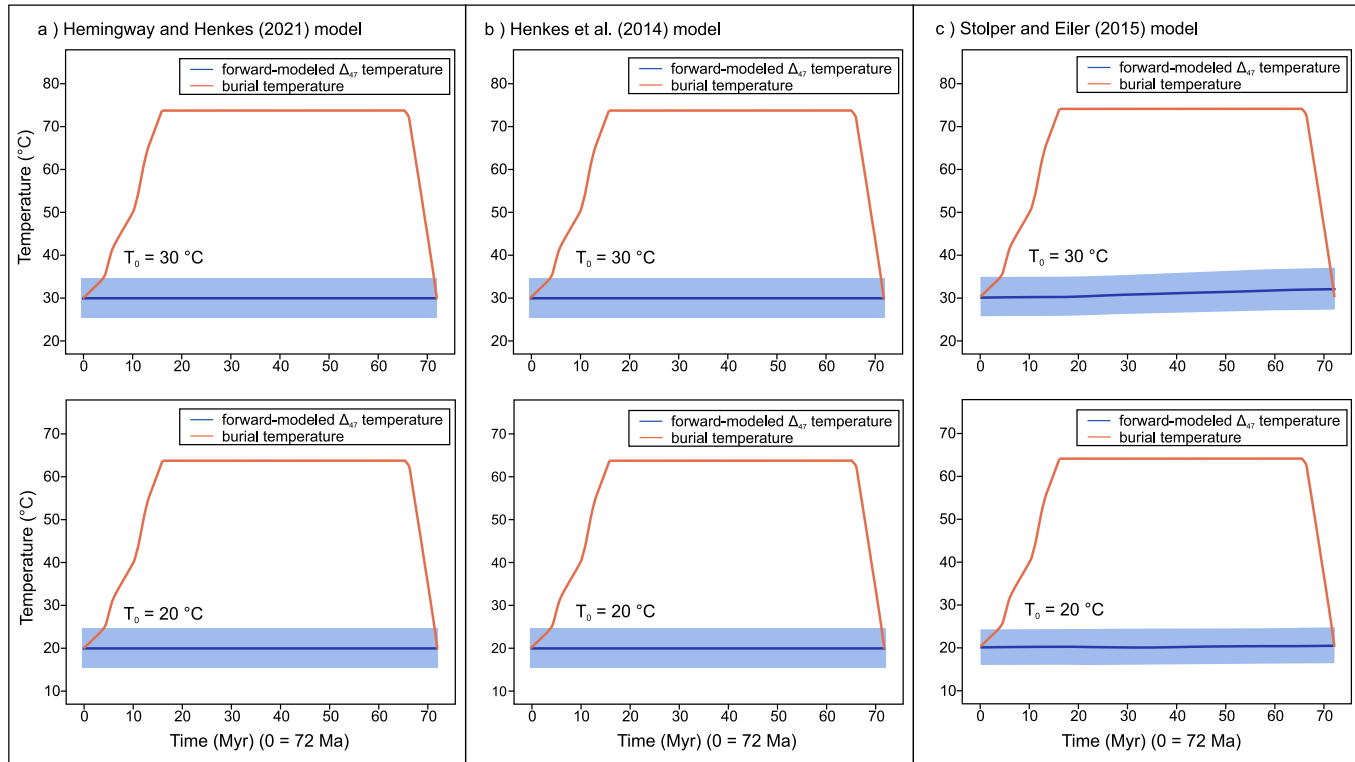


**Fig. 5.** Solid-state reordering modelings by using models from (a) Hemingway and Henkes (2021), (b) Henkes et al. (2014), (c) Stolper and Eiler (2015). The burial history is inferred from Zhang et al. (2013) and Xi et al. (2015), with a maximum burial temperature ( $T_{\max}$ ) of 65–75 °C lasted for 50 Myrs and an initial depositional temperature ( $T_0$ ) of 20–30 °C. All the model-scenario combinations produce negligible reordering of  $T(\Delta_{47})$  (<3 °C), which suggests that our dense micrite samples would not be altered by solid-state reordering. The modelings are performed by the open source ‘isotopylog’ module written in python (Hemingway, 2020; <http://pypi.python.org/pypi/isotopylog>).

vertebrates would prefer a comfortable environment in which they could survive (Sun et al., 2012). Furthermore, in low latitudes, the precipitation also serves as the main controller of the meteoric water  $\delta^{18}\text{O}$  values (Amiot et al., 2004; Fricke and O'Neil, 1999) and may introduce errors in the calculation of biogenic temperatures from the meteoric water  $\delta^{18}\text{O}$  values (Dworkin et al., 2005; Fricke and O'Neil, 1999).

Recently, the substantially high low-latitude terrestrial temperatures were also recognized in other greenhouse periods. For example, Naafs et al. (2018) suggested a low-latitude terrestrial temperature of  $>30\text{ }^{\circ}\text{C}$  significantly during PETM based on the brGDGTs. According to the siderite clumped isotope geothermometer, Van Dijk et al. (2020) also reported an extremely high equatorial mean annual temperatures of  $41\text{ }^{\circ}\text{C}$  on land during the PETM. These extremely high land surface temperatures during the PETM correlate well with marine temperatures and the latest climate simulations (Tierney et al., 2022; Zhu et al., 2019), which implies that many low-latitude terrestrial temperatures were underestimated.

For the K-Pg boundary interval, only few of low-latitude terrestrial temperatures were reconstructed (Zhang et al., 2019), and non-negligible incongruities still exist between proxy and model temperatures (Niegzodzki et al., 2017). The best fit of the proxy data is obtained by climate simulation with  $\text{CO}_2$  of 560–1120 ppm in mid and high latitudes, while the simulated temperatures with  $\text{CO}_2$  of 280 ppm more close the proxy data in the tropics (Niegzodzki et al., 2017). The previous studies suggested that the overestimate of the low-latitude temperatures in climate models should be blamed for this inconsistency. Our result in the Nanxiong Basin resolves the inconsistency by representing the first pronounced terrestrial high-temperature record in the low latitudes during the K-Pg boundary interval (Fig. 6a). It is consistent with the low-latitude sea surface temperatures during this period (Zhang et al., 2019). It also fits well with the simulated low-latitude temperatures with 560–840 ppm  $\text{CO}_2$ , which is consistent with the  $p\text{CO}_2$  reconstruction of 1058 ppm based on  $\delta^{13}\text{C}$  of paleosol carbonates and 665–1143 ppm based on leaf gas-exchange (Milligan et al., 2022; Zhang et al., 2018).

According to Zhang et al. (2016b), the “Tropical” climate (MAAT  $> 23\text{ }^{\circ}\text{C}$ ) is assigned to the Nanxiong Basin (MAAT =  $30\text{ }^{\circ}\text{C}$ ) during the K-

Pg boundary interval, which means the north bound of the tropics would be far beyond  $25\text{ }^{\circ}\text{N}$  during this period (Fig. 6b). According to the Global Summary of the Year (GSOY), the present MAATs are  $29\text{ }^{\circ}\text{C}$  in Thailand (“Tropical” climate;  $14\text{ }^{\circ}\text{N}$ ),  $25\text{ }^{\circ}\text{C}$  in Hainan (“Tropical” climate;  $20\text{ }^{\circ}\text{N}$ ), and  $21\text{ }^{\circ}\text{C}$  in the Nanxiong Basin (“Temperate” climate;  $24\text{ }^{\circ}\text{N}$ ) (Lawrimore et al., 2016), which strongly supports hotter equatorial regions and expanded tropics during the K-Pg boundary interval.

### 5.3. Mercury signal and its possible climatic forcing

During volcanic eruptions, a large amount of mercury is released into the atmosphere and deposit to the sediment within 0.5–2 years (Pyle and Mather, 2003), which leads to anomalously high mercury levels in sediments. Previous studies have already identified globally distributed Hg anomalies across the K-Pg boundary caused by DT eruptions (Font et al., 2016; Font et al., 2022; Gu et al., 2022; Keller et al., 2020; Li et al., 2022; Meyer et al., 2019). In the Nanxiong Basin, Ma et al. (2022) linked the Hg anomalies to the DT eruptions by high-resolution Hg isotopic analysis, which is consistent with other heavy metals concentration anomalies (e.g., Co & Cd). However, all the Hg spikes in the Datang section of the Nanxiong Basin are relatively low (i.e.,  $< 20\text{ ppb}$ ). In contrast, although the Songliao Basin in NE China was more distal from the DT than the Nanxiong Basin (Gu et al., 2022), the Hg spikes are much higher (i.e.,  $64\text{ ppb}$ ) (Fig. 7). We, therefore, speculate that mercury released by the DT may not be well sequestered in the Nanxiong Basin.

Mercury enters lakes via two pathways: (1) Direct atmospheric deposition via precipitation, and (2) surface runoff of soil (Amos et al., 2014; Grasby et al., 2019). Ma et al. (2022) suggested that Hg sequestration around the main spike in the Nanxiong Basin could be attributed to the supply of atmospheric Hg linked to the volcanism. As a small intermontane basin, the catchment and lake surface areas in the basin are small (Wang, 2012). Both the clay mineral combinations and the abundant pedogenic carbonate nodules and paleosol layers in the Nanxiong Basin suggest a low-precipitation and high-evaporation arid climate during this period (Wang, 2012). Meanwhile, in arid areas, soil contain low Hg concentrations due to the lack of vegetation cover. All in all, we conclude that in the context of hot and arid regional climate, the mercury sequestration was constrained to a low level in the Nanxiong

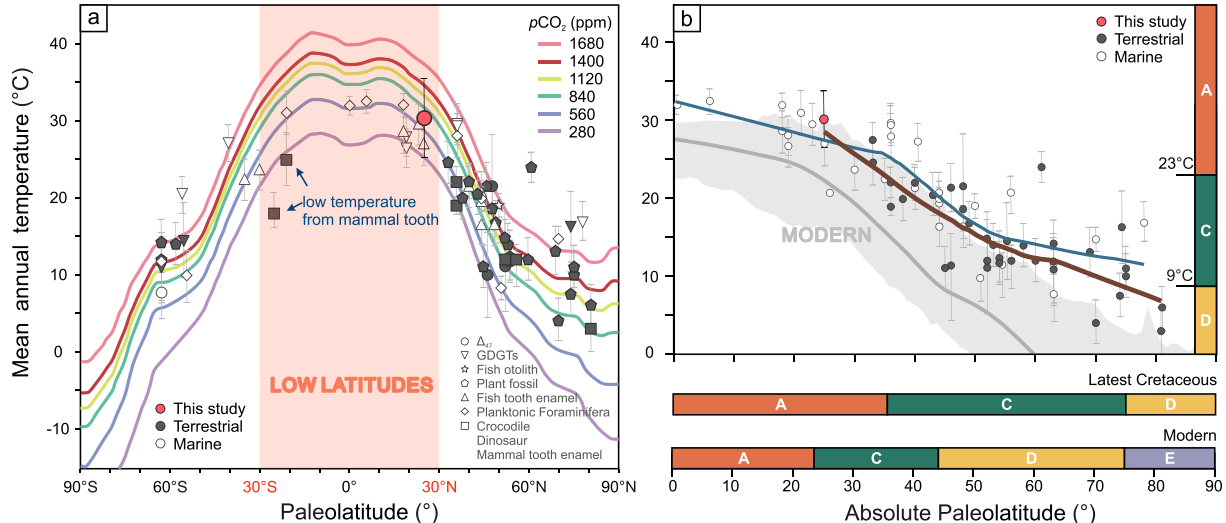


**Fig. 6.** Compilation of latest Cretaceous temperature estimates. (a) Terrestrial and marine temperature estimates and climate model's latitudinal mean temperature. The model results for the latest Cretaceous are derived from Niegzodzki et al. (2017) by using the atmosphere-ocean general circulation model (AOGCM). All the published proxy estimates data are derived from Zhang et al. (2019). Vertical gray lines across the temperature estimates symbols represent  $\pm 1\sigma$  deviation. (b) The latitudinal temperature gradients for the land and ocean, and the climate belts during the latest Cretaceous and modern eras. Terrestrial and marine latitudinal temperature gradients are denoted as brown and blue lines, respectively. Orange = A (Tropical); Green = C (Temperate); Yellow = D (Cold); Purple = E (Polar). The climate belts are classified according to Zhang et al. (2016b). Vertical gray lines across the temperature estimates symbols represent  $\pm 1\sigma$  deviation. (For interpretation of the references to colour in this figure legend, the reader is referred to the web version of this article.)

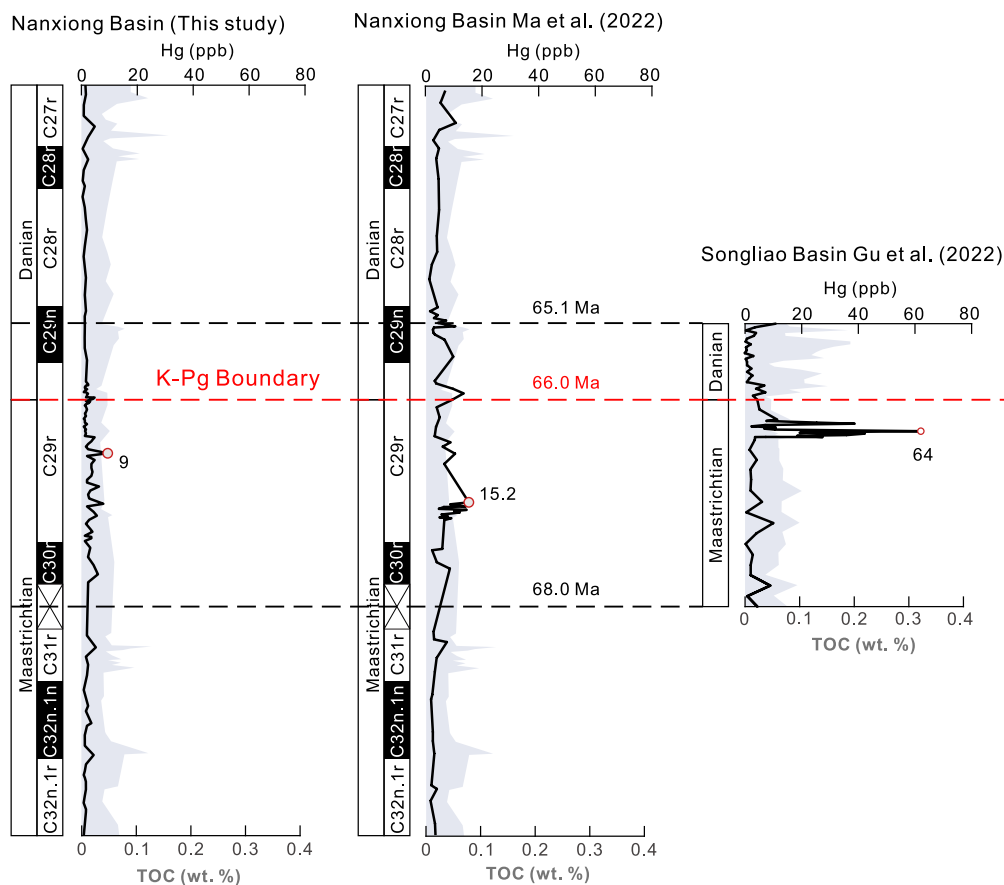


**Fig. 7.** Sedimentary mercury records in the Nanxiong Basin and Songliao Basin during the K-Pg boundary interval. The shadows represent the TOC values.

Basin during the K-Pg boundary interval.

## 6. Conclusions

By analyzing the clumped isotope concentrations ( $\Delta_{47}$ ) and total mercury signals of sediments in the Nanxiong Basin, South China, we present the first quantitative low-latitude terrestrial high-temperature record during the K-Pg boundary interval.

Our study suggests an extremely high MAAT of  $30 \pm 4^\circ\text{C}$  during the K-Pg boundary interval in the low-latitude Nanxiong Basin, which corresponds to the coeval SST reconstructions and the modeling results and emphasizes the role of low-latitude continent in the global heat transport. The significant tropical expand during the K-Pg boundary interval implies that the biotas may have been massively impacted by the hot climate. The THg analysis shows that the mercury sequestration in the Nanxiong Basin during DT eruptions was constrained to a low level due to the hot and arid regional climate.

## Declaration of Competing Interest

The authors declare that they have no known competing financial interests or personal relationships that could have appeared to influence the work reported in this paper.

## Data availability

All new data from this study are available in the Supplementary Data files; previously published data are available from the referenced works.

## Acknowledgements

We thank two anonymous reviewers for detailed and constructive reviews. This work was financially supported by the National Natural Science Foundation of China [grants 41888101 and 42072116], the Chinese “111” project [grant B20011], and the Fundamental Research Funds for the Central Universities [grant 2652021094].

## Appendix A. Supplementary data

Supplementary data to this article can be found online at <https://doi.org/10.1016/j.palaeo.2023.111489>.

## References

- Amiot, R., Lécuyer, C., Buffetaut, E., Fluteau, F., Legendre, S., Martineau, F., 2004. Latitudinal temperature gradient during the cretaceous Upper Campanian-Middle Maastrichtian: 818O record of continental vertebrates. *Earth Planet. Sci. Lett.* 226, 255–272.
- Amos, H.M., Jacob, D.J., Kocman, D., Horowitz, H.M., Zhang, Y., Dutkiewicz, S., Horvat, M., Corbitt, E.S., Krabbenhoft, D.P., Sunderland, E.M., 2014. Global biogeochemical implications of mercury discharges from rivers and sediment burial. *Environ. Sci. Technol.* 48, 9514–9522.
- Anderson, N.T., Kelson, J.R., Kele, S., Daëron, M., Bonifacie, M., Horita, J., Mackey, T.J., John, C.M., Kluge, T., Petschnig, P., Jost, A.B., Huntington, K.W., Bernasconi, S.M., Bergmann, K.D., 2021. A Unified Clumped Isotope Thermometer Calibration (0.5–1,100°C) using Carbonate-based Standardization. *Geophys. Res. Lett.* 48, e2020GL092069.
- Banner, J.L., Hanson, G.N., 1990. Calculation of simultaneous isotopic and trace element variations during water-rock interaction with applications to carbonate diagenesis. *Geochim. Cosmochim. Acta* 54, 3123–3137.
- Barnet, J.S.K., Littler, K., Kroon, D., Leng, M.J., Westerhold, T., Röhli, U., Zachos, J.C., 2017. A new high-resolution chronology for the late Maastrichtian warming event: establishing robust temporal links with the onset of Deccan volcanism. *Geology* 46, 147–150.

- Burgener, L., Hyland, E., Huntington, K.W., Kelson, J.R., Sewall, J.O., 2019. Revisiting the equitable climate problem during the late cretaceous greenhouse using paleosol carbonate clumped isotope temperatures from the Campanian of the Western Interior Basin, USA. *Palaeogeogr. Palaeoclimatol. Palaeoecol.* 516, 244–267.
- Chen, Z., Cheng, J., Guo, P., Lin, Z., Zhang, F., 2010. Distribution characters and its control factors of stable isotope in precipitation over china (in Chinese with English abstract). *Trans. Atmos. Sci.* 33, 667–679.
- Clyde, William C., Ting, S., Snell, Kathryn E., Bowen, Gabriel J., Tong, Y., Koch, Paul L., Li, Q., Wang, Y., 2010. New paleomagnetic and stable-isotope results from the Nanxiong Basin, China: Implications for the K/T boundary and the timing of Paleocene mammalian turnover. *J. Geol.* 118, 131–143.
- Dennis, K.J., Affek, H.P., Passey, B.H., Schrag, D.P., Eiler, J.M., 2011. Defining an absolute reference frame for 'clumped' isotope studies of CO<sub>2</sub>. *Geochim. Cosmochim. Acta* 75, 7117–7131.
- Drise, S.G., Mora, C.I., 1993. Physico-chemical environment of pedogenic carbonate formation in Devonian vetric palaeosols, Central Appalachians, USA. *Sedimentology* 40, 199–216.
- Dworkin, S.I., Nordt, L., Atchley, S., 2005. Determining terrestrial paleotemperatures using the oxygen isotopic composition of pedogenic carbonate. *Earth Planet. Sci. Lett.* 237, 56–68.
- Farnsworth, A., Lunt, D.J., Robinson, S.A., Valdes, P.J., Roberts, W.H.G., Clift, P.D., Markwick, P., Su, T., Wrobel, N., Bragg, F., Kelland, S.-J., Pancost, R.D., 2019. Past East Asian monsoon evolution controlled by paleogeography, not CO<sub>2</sub>. *Sci. Adv.* 5, eaax1697.
- Font, E., Adatte, T., Sial, A.N., Drude de Lacerda, L., Keller, G., Punekar, J., 2016. Mercury anomaly, Deccan volcanism, and the end-cretaceous mass extinction. *Geology* 44, 171–174.
- Font, E., Chen, J., Regelous, M., Regelous, A., Adatte, T., 2022. Volcanic origin of the mercury anomalies at the Cretaceous-Paleogene transition of Bidart, France. *Geology* 50, 142–146.
- Fricke, H.C., O'Neil, J.R., 1999. The correlation between 18O/16O ratios of meteoric water and surface temperature: its use in investigating terrestrial climate change over geologic time. *Earth Planet. Sci. Lett.* 170, 181–196.
- Gao, Y., Ibarra, D.E., Wang, C., Caves, J.K., Chamberlain, C.P., Graham, S.A., Wu, H., 2015. Mid-latitude terrestrial climate of East Asia linked to global climate in the late cretaceous. *Geology* 43, 287–290.
- Ghosh, P., Adkins, J., Affek, H., Balta, B., Guo, W., Schauble, E.A., Schrag, D., Eiler, J.M., 2006. 13C–18O bonds in carbonate minerals: a new kind of paleothermometer. *Geochim. Cosmochim. Acta* 70, 1439–1456.
- Gilabert, V., Batenburg, S.J., Arenillas, I., Arz, J.A., 2022. Contribution of orbital forcing and Deccan volcanism to global climatic and biotic changes across the Cretaceous–Paleogene boundary at Zumia, Spain. *Geology* 50, 21–25.
- Grasby, S.E., Them II, T.R., Chen, Z., Yin, R., Ardakani, O.H., 2019. Mercury as a proxy for volcanic emissions in the geologic record. *Earth Sci. Rev.* 196, 102880.
- Green, T., Renne, P.R., Keller, C.B., 2022. Continental flood basalts drive Phanerozoic extinctions. *Proc. Natl. Acad. Sci.* 119, e2120441119.
- Gu, X., Zhang, L., Yin, R., Grasby, S.E., Yao, H., Tan, J., Wang, C., 2022. Deccan volcanic activity and its links to the end-cretaceous extinction in northern China. *Glob. Planet. Chang.* 210, 103772.
- Hemingway, J.D., 2020. isotopylog: open-source tools for clumped isotope kinetic data analysis, 2020 [online; accessed 2022-10-06]. <http://pypi.python.org/pypi/isotopylog>.
- Hemingway, J.D., Henkes, G.A., 2021. A disordered kinetic model for clumped isotope bond reordering in carbonates. *Earth Planet. Sci. Lett.* 566, 116962.
- Henkes, G.A., Passey, B.H., Grossman, E.L., Shenton, B.J., Pérez-Huerta, A., Yancey, T.E., 2014. Temperature limits for preservation of primary calcite clumped isotope paleotemperatures. *Geochim. Cosmochim. Acta* 139, 362–382.
- Henkes, G.A., Passey, B.H., Grossman, E.L., Shenton, B.J., Yancey, T.E., Pérez-Huerta, A., 2018. Temperature evolution and the oxygen isotope composition of Phanerozoic oceans from carbonate clumped isotope thermometry. *Earth Planet. Sci. Lett.* 490, 40–50.
- Huang, C., Retallack, G.J., Wang, C., Huang, Q., 2013. Paleoatmospheric pCO<sub>2</sub> fluctuations across the Cretaceous-Tertiary boundary recorded from paleosol carbonates in NE China. *Palaeogeogr. Palaeoclimatol. Palaeoecol.* 385, 95–105.
- Huber, M., 2008. A hotter greenhouse? *Science* 321, 353–354.
- Hull, P.M., Bornemann, A., Pennman, D.E., Henehan, M.J., Norris, R.D., Wilson, P.A., Blum, P., Alegret, L., Batenburg, S.J., Bow, P.R., Bralower, T.J., Courneille, C., Deutsch, A., Donner, B., Friedrich, O., Jehle, S., Kim, H., Kroon, D., Lippert, P.C., Loroch, D., Moebius, I., Moriya, K., Peppe, D.J., Ravizza, G.E., Röhl, U., Schueth, J., Sepulveda, J., Sexton, P.F., Sibert, E.C., Śliwińska, K.K., Summons, R.E., Thomas, E., Westerhold, T., Whiteside, J.H., Yamaguchi, T., Zachos, J.C., 2020. On impact and volcanism across the Cretaceous-Paleogene boundary. *Science* 367, 266–272.
- Huntington, K.W., Lechner, A.R., 2015. Carbonate clumped isotope thermometry in continental tectonics. *Tectonophysics* 647–648, 1–20.
- Huth, T.E., Cerling, T.E., Marchetti, D.W., Bowring, D.R., Ellwein, A.L., Passey, B.H., 2019. Seasonal bias in soil carbonate formation and its implications for interpreting high-resolution paleoarchives: evidence from Southern Utah. *J. Geophys. Res. Biogeosci.* 124, 616–632.
- Inglis, G.N., Farnsworth, A., Lunt, D., Foster, G.L., Hollis, C.J., Pagani, M., Jardine, P.E., Pearson, P.N., Markwick, P., Galsworthy, A.M.J., Raynham, L., Taylor, K.W.R., Pancost, R.D., 2015. Descent toward the Icehouse: Eocene Sea surface cooling inferred from GDGT distributions. *Paleoceanography* 30, 1000–1020.
- John, C.M., 2018. Burial estimates constrained by clumped isotope thermometry: example of the lower cretaceous Qishn Formation (Haushi-Huqf High, Oman). *Geol. Soc. Lond. Spec. Publ.* 435, 107–121.
- Jones, M.M., Petersen, S.V., Curley, A.N., 2022. A tropically hot mid-cretaceous north American Western Interior Seaway. *Geology* 50, 954–958.
- Keller, G., Mateo, P., Monkenbusch, J., Thibault, N., Punekar, J., Spangenberg, J.E., Abramovich, S., Ashkenazi-Polivoda, S., Schoene, B., Eddy, M.P., Samperton, K.M., Khadri, S.F.R., Adatte, T., 2020. Mercury linked to Deccan Traps volcanism, climate change and the end-cretaceous mass extinction. *Glob. Planet. Chang.* 194, 103312.
- Kelson, J.R., Huntington, K.W., Breecker, D.O., Burgener, L.K., Gallagher, T.M., Hoke, G.D., Petersen, S.V., 2020. A proxy for all seasons? A synthesis of clumped isotope data from Holocene soil carbonates. *Quat. Sci. Rev.* 234, 106259.
- Kim, S.-T., O'Neil, J.R., 1997. Equilibrium and nonequilibrium oxygen isotope effects in synthetic carbonates. *Geochim. Cosmochim. Acta* 61, 3461–3475.
- Klages, J.P., Salzmann, U., Bickert, T., Hillenbrand, C.-D., Gohl, K., Kuhn, G., Bohaty, S.M., Titschack, J., Müller, J., Frederichs, T., Bauersachs, T., Ehrmann, W., van de Flierdt, T., Pereira, P.S., Larter, R.D., Lohmann, G., Niezgodzki, I., Uenzelmann-Neben, G., Zundel, M., Spiegel, C., Mark, C., Chew, D., Francis, J.E., Nehrke, G., Schwarz, F., Smith, J.A., Freudenthal, T., Esper, O., Pälike, H., Ronge, T.A., Dziadek, R., Ananasyeva, V., Arndt, J.E., Ebermann, B., Gebhardt, C., Hochmuth, K., Küssner, K., Najman, Y., Rieftahl, F., Scheinert, M., the Science Team of Expedition, 2020. Temperate rainforests near the South Pole during peak Cretaceous warmth. *Nature* 580, 81–86.
- Kongchum, M., Hudnall, W.H., Delaune, R.D., 2011. Relationship between sediment clay minerals and total mercury. *J. Environ. Sci. Health A* 46, 534–539.
- Kraus, M.J., 1999. Paleosols in clastic sedimentary rocks: their geologic applications. *Earth Sci. Rev.* 47, 41–70.
- Laugé, M., Donnadieu, Y., Ladant, J.B., Green, J.A.M., Bopp, L., Raisson, F., 2020. Stripping back the modern to reveal the Cenomanian-Turonian climate and temperature gradient underneath. *Clim. Past* 16, 953–971.
- Lawrimore, J.H.R., Applequist, R., Korzeniewski, S., Menne, B., Matthew, J., 2016. Global Summary of the Year (GSOY), Version 1. NOAA National Centers for Environmental Information.
- Li, G., Hirano, H., Batten, D.J., Wan, X., Willem, H., Zhang, X., 2010. Biostratigraphic significance of spinicardatans from the Upper cretaceous Nanxiong Group in Guangdong, South China. *Cretac. Res.* 31, 387–395.
- Li, S., Grasby, S.E., Zhao, X., Chen, J., Zheng, D., Wang, H., Fang, Y., Zhang, Q., Yu, T., Tian, J., Du, S., Jarzembski, E.A., Wang, Q., Zhang, H., Wan, X., Wang, B., 2022. Mercury evidence of Deccan volcanism driving the latest Maastrichtian warming event. *Geology* 50, 1140–1144.
- Ma, M., Liu, X., Wang, W., 2018. Palaeoclimate evolution across the Cretaceous–Palaeogene boundary in the Nanxiong Basin (SE China) recorded by red strata and its correlation with marine records. *Clim. Past* 14, 287–302.
- Ma, M., Zhang, W., Zhao, M., Qiu, Y., Cai, H., Chen, J., Liu, X., 2022. Deccan Traps Volcanism Implicated in the Extinction of Non-Avian Dinosaurs in Southeastern China. *Geophys. Res. Lett.* 49, e2022GL100342.
- Meyer, K.W., Petersen, S.V., Lohmann, K.C., Blum, J.D., Washburn, S.J., Johnson, M.W., Gleason, J.D., Kurz, A.Y., Winkelstern, I.Z., 2019. Biogenic carbonate mercury and marine temperature records reveal global influence of late cretaceous Deccan Traps. *Nat. Commun.* 10, 5356.
- Milligan, J.N., Flynn, A.G., Kowalczyk, J.B., Barclay, R.S., Geng, J., Royer, D.L., Peppe, D.J., 2022. Moderate to elevated atmospheric CO<sub>2</sub> during the early Paleocene recorded by platianites leaves of the San Juan Basin, New Mexico. *Paleoceanogr. Paleoclimatol.* 37, e2021PA004408.
- Naafs, B.D.A., Rohrssen, M., Inglis, G.N., Lähteenoja, O., Feakins, S.J., Collinson, M.E., Kennedy, E.M., Singh, P.K., Singh, M.P., Lunt, D.J., Pancost, R.D., 2018. High temperatures in the terrestrial mid-latitudes during the early Palaeogene. *Nat. Geosci.* 11, 766–771.
- Niezgodzki, I., Knorr, G., Lohmann, G., Tyszka, J., Markwick, P.J., 2017. Late cretaceous climate simulations with different CO<sub>2</sub> levels and subarctic gateway configurations: a model-data comparison. *Paleoceanography* 32, 980–998.
- Passey, B.H., Henkes, G.A., 2012. Carbonate clumped isotope bond reordering and geospeedometry. *Earth Planet. Sci. Lett.* 351–352, 223–236.
- Passey, B.H., Levin, N.E., Cerling, T.E., Brown, F.H., Eiler, J.M., 2010. High-temperature environments of human evolution in East Africa based on bond ordering in paleosol carbonates. *Proc. Natl. Acad. Sci.* 107, 11245–11249.
- Percival, L.M.E., Witt, M.L.I., Mather, T.A., Hermoso, M., Jenkyns, H.C., Hesselbo, S.P., Al-Suwaidi, A.H., Storm, M.S., Xu, W., Ruhl, M., 2015. Globally enhanced mercury deposition during the end-Pliensbachian extinction and Toarcian OAE: a link to the Karoo-Ferrar large Igneous Province. *Earth Planet. Sci. Lett.* 428, 267–280.
- Petersen, S.V., Tabor, C.R., Lohmann, K.C., Poulsen, C.J., Meyer, K.W., Carpenter, S.J., Erickson, J.M., Matsunaga, K.K., Smith, S.Y., Sheldon, N.D., 2016. Temperature and salinity of the late cretaceous western interior seaway. *Geology* 44, 903–906.
- Pyle, D.M., Mather, T.A., 2003. The importance of volcanic emissions for the global atmospheric mercury cycle. *Atmos. Environ.* 37, 5115–5124.
- Robinson, A.S., Dale, A., Adatte, T., John, C.M., 2022. Cenozoic sediment bypass versus Laramide exhumation and erosion of the Eagle Ford Group: Perspective from modelling of organic and inorganic proxy data (Maverick Basin, Texas, USA). *Geology* 50, 817–821.
- Scoates, C.R., 2021. An Atlas of Phanerozoic Paleogeographic Maps: the Seas come in and the Seas Go out. *Annu. Rev. Earth Planet. Sci.* 49, 679–728.
- Snell, K.E., Thrasher, B.L., Eiler, J.M., Koch, P.L., Sloan, L.C., Tabor, N.J., 2013. Hot summers in the Bighorn Basin during the early Paleogene. *Geology* 41, 55–58.
- Stolper, D.A., Eiler, J.M., 2015. The kinetics of solid-state isotope-exchange reactions for clumped isotopes: a study of inorganic calcites and apatites from natural and experimental samples. *Am. J. Sci.* 315, 363.
- Sun, Y., Joachims, M.M., Wignall, P.B., Yan, C., Chen, Y., Jiang, H., Wang, L., Lai, X., 2012. Lethally Hot Temperatures during the early Triassic Greenhouse. *Science* 338, 366–370.

- Tierney, J.E., Poulsen Christopher, J., Montañez Isabel, P., Bhattacharya, T., Feng, R., Ford Heather, L., Hönsch, B., Inglis Gordon, N., Petersen Sierra, V., Sagoo, N., Tabor Clay, R., Thirumalai, K., Zhu, J., Burls Natalie, J., Foster Gavin, L., Goddérus, Y., Huber Brian, T., Ivany Linda, C., Kirtland Turner, S., Lunt Daniel, J., McElwain Jennifer, C., Mills Benjamin, J.W., Otto-Btiesner Bette, L., Ridgwell, A., Zhang Yi, G., 2020. Past climates inform our future. *Science* 370, eaay3701.
- Tierney, J.E., Zhu, J., Li, M., Ridgwell, A., Hakim, G.J., Poulsen, C.J., Whiteford, R.D.M., Rae, J.W.B., Kump, L.R., 2022. Spatial patterns of climate change across the Paleocene-Eocene Thermal Maximum. *Proc. Natl. Acad. Sci.* 119, e2205326119.
- Upchurch, J., Garland, R., Kiehl, J., Shields, C., Scherer, J., Scotese, C., 2015. Latitudinal temperature gradients and high-latitude temperatures during the latest cretaceous: Congruence of geologic data and climate models. *Geology* 43, 683–686.
- Van Dijk, J., Fernandez, A., Bernasconi, S.M., Caves Rugenstein, J.K., Passey, S.R., White, T., 2020. Spatial pattern of super-greenhouse warmth controlled by elevated specific humidity. *Nat. Geosci.* 13, 739–744.
- Wang, P., 2006. Orbital forcing of the low-latitude processes (in Chinese with English abstract). *Quat. Sci.* 26, 694–701.
- Wang, Y., 2012. Paleoclimate Changes of the Late Cretaceous - Early Paleocene in the Nanxiong Basin. Nanjing University, South China.
- Westerhold, T., Marwan, N., Drury, A.J., Liebrand, D., Agnini, C., Anagnostou, E., Barnet, J.S.K., Bohaty, S.M., De Vleeschouwer, D., Florindo, F., Frederichs, T., Hodell, D.A., Holbourn, A.E., Kroon, D., Lauretano, V., Littler, K., Lourens, L.J., Lyle, M., Pälike, H., Röhl, U., Tian, J., Wilkens, R.H., Wilson, P.A., Zachos, J.C., 2020. An astronomically dated record of Earth's climate and its predictability over the last 66 million years. *Science* 369, 1383–1387.
- Westerhold, T., Röhl, U., Donner, B., McCarren, H.K., Zachos, J.C., 2011. A complete high-resolution Paleocene benthic stable isotope record for the Central Pacific (ODP Site 1209). *Paleoceanography* 26, PA2216.
- Xi, Y., Wang, Y., Hu, X., Liu, S., Zhao, Y., Liu, T., 2015. Geothermal structure revealed by Curie isotherm surface in Guangdong province. In: International Workshop and Gravity, Electrical & Magnetic Methods and their Applications, Chengdu, China, 19–22 April 2015, pp. 189–192.
- Yan, Y., Xia, B., Lin, G., Cui, X., Hu, X., Yan, P., Zhang, F., 2007. Geochemistry of the sedimentary rocks from the Nanxiong Basin, South China and implications for provenance, paleoenvironment and paleoclimate at the K/T boundary. *Sediment. Geol.* 197, 127–140.
- Zhang, L., Hay, W.W., Wang, C., Gu, X., 2019. The evolution of latitudinal temperature gradients from the latest cretaceous through the present. *Earth Sci. Rev.* 189, 147–158.
- Zhang, L., Wang, C., Cao, K., Wang, Q., Tan, J., Gao, Y., 2016a. High elevation of Jiaolai Basin during the late cretaceous: Implication for the coastal mountains along the East asian margin. *Earth Planet. Sci. Lett.* 456, 112–123.
- Zhang, L., Wang, C., Li, X., Cao, K., Song, Y., Hu, B., Lu, D., Wang, Q., Du, X., Cao, S., 2016b. A new paleoclimate classification for deep time. *Palaeogeogr. Palaeoclimatol. Palaeoecol.* 443, 98–106.
- Zhang, L., Wang, C., Wignall, P.B., Kluge, T., Wan, X., Wang, Q., Gao, Y., 2018. Deccan volcanism caused coupled pCO<sub>2</sub> and terrestrial temperature rises, and pre-impact extinctions in northern China. *Geology* 46, 271–274.
- Zhang, L., Yin, Y., Wang, C., 2021. High-altitude and cold habitat for the early cretaceous feathered dinosaurs at Sihetun, Western Liaoning, China. *Geophys. Res. Lett.* 48, e2021GL094370.
- Zhang, X., Lin, J., Li, G., Ling, Q., 2006. Non-marine Cretaceous-Paleogene boundary section at Datang of Nanxiong, Northern Guangdong (in Chinese with English abstract). *J. Stratigr.* 23, 327–340.
- Zhang, X., Zhang, X., Hou, M., Li, G., Li, H., 2013. Lithostratigraphic subdivision of red beds in Nanxiong Basin, Guangdong, China (in Chinese with English abstract). *J. Stratigr.* 37, 441–451.
- Zhao, M., Ma, M., He, M., Qiu, Y., Liu, X., 2021. Evaluation of the four potential Cretaceous-Paleogene (K-Pg) boundaries in the Nanxiong Basin based on evidences from volcanic activity and paleoclimatic evolution. *Sci. China Earth Sci.* 64, 631–641.
- Zhu, J., Poulsen, C.J., Tierney, J.E., 2019. Simulation of Eocene extreme warmth and high climate sensitivity through cloud feedbacks. *Sci. Adv.* 5, eaax1874.